Journal of Alloys and Compounds 959 (2023) 170583

Contents lists available at ScienceDirect

Journal of Alloys and Compounds

journal homepage: www.elsevier.com/locate/jalcom

Anharmonicity effects and thermal expansion of thermoelectric (M,M',M")NiSn (M,M',M"=Ti, Zr, Hf) half-Heusler alloys

C. Echevarria-Bonet [a,b,*,1], J.L. Garrido-Alvarez [b], D. Martinez-Blanco [c], P. Gorria [d], M.H. Sørby [a], M.D. Riktor [e], J.A. Blanco [b], B.C. Hauback [a]

[a] Department for Hydrogen Technology, Institute for Energy Technology (IFE), P.O. Box 40, N-2027 Kjeller, Norway
[b] Department of Physics & MAGNES, University of Oviedo, 33007 Oviedo, Spain
[c] Scientific-Technical Services, University of Oviedo, 33006 Oviedo, Spain
[d] Department of Physics & IUTA, EPI, University of Oviedo, 33203 Gijón, Spain
[e] SINTEF Materials and Chemistry, P.O. Box 124, N-0316 Oslo, Norway

ARTICLE INFO

Article history:
Received 22 March 2023
Received in revised form 12 May 2023
Accepted 14 May 2023
Available online 18 May 2023

Keywords:
Thermoelectric
Half-Heusler
Synchrotron x-ray powder diffraction
Linear thermal expansion
Debye temperature
Anharmonicity

ABSTRACT

High-resolution synchrotron radiation X-ray powder diffraction was used for the structural characterization of half-Heusler alloys with compositions MNiSn, $M_{0.5}M'_{0.5}$NiSn, and $M_{0.5}M'_{0.25}M"_{0.25}$NiSn ((M, M', M") = Ti, Zr, Hf). These alloys were synthesized by arc melting and subsequent thermal annealing. Rietveld refinements of the room temperature patterns revealed that the unit cell parameter is larger for ZrNiSn and smaller for TiNiSn, in accordance with the respective atomic radii. The site occupation of each atomic species exhibited similar trends to those reported in the literature. The values of the linear coefficient of thermal expansion (α) for all the investigated phases within the alloys are $< 10^{-5}$ K^{-1}. In addition, the value of the Debye temperature (θ_D) is estimated by analyzing the temperature dependence of the isotropic atomic displacement parameters. In the case of these half-Heusler alloys, it is observed that a lower θ_D corresponds to a lower α. The good agreement between the temperature dependence of the Debye temperature and the calculated values using the Thirring-Stern expansion enables us to demonstrate the significant role of anharmonicity: the lighter the compound, the lower the anharmonicity. Furthermore, we also discuss the implications of anharmonicity on the thermal conductivity of this family of half-Heusler compounds at room temperature.

1. Introduction

There is a global need for new energy sources and methods of energy conversion. Thermoelectric (TE) materials have the potential to fulfill this need [1]. The TE effect enables the conversion of a temperature gradient into an electric current. Consequently, waste heat, such as that from a car exhaust or industrial processes, can be efficiently transformed into usable electric energy, thereby enhancing overall system energy efficiency [2].

Among the various TE materials, BiTe- and PbTe-based alloys have been extensively studied due to their promising properties, particularly their high efficiency. The efficiency of TE materials is closely associated with their TE figure of merit, zT,

$$zT = \frac{S^2\sigma}{\kappa}T \quad (1)$$

where S is the Seebeck coefficient, σ the electrical conductivity and κ the thermal conductivity. However, due to toxicity concerns or their inclusion in the critical raw materials (CRM) list [3,4], some of the atomic species used (such as Te and Pb) should be replaced with alternative options. In this regard, half-Heusler (hH) alloys have gained significant attention in recent years as potential alternatives for TE generators. These hH alloys exhibit high performance, good stability at high temperatures (high melting point values), low toxicity and mechanical robustness. Moreover, they are composed of inexpensive and abundant constituents [5]. Importantly, these alloys are semiconductors with a narrow band gap in the density of states, a crucial characteristic for their application in TE systems. XYZ hH alloys adopt the MgAgAs-type crystal structure with space group *F*-43*m* (no. 216), being X and Y transition metals, such as X = Ti, Zr, Hf and Y = Co, Ni, Fe, while Z is a *sp*-metalloid or metal, such as Z = Sn, Sb, Bi. The crystal structure of hH alloys can be derived through the

* Corresponding author at: Department of Physics & MAGNES, University of Oviedo, 33007 Oviedo, Spain.
E-mail address: echevarriacristina@uniovi.es (C. Echevarria-Bonet).
[1] ORCID(s): 0000-0001-8323-9225

https://doi.org/10.1016/j.jallcom.2023.170583

interpenetration of a rocksalt- and a zincblende-type crystal structures. The elements X and Z are located at the Wyckoff positions of the rock-salt crystal structure 4a (0,0,0) and 4b (1/2,1/2,1/2), respectively. The elements X and Y form the zincblende structure occupying the positions 4a (0,0,0) and 4c (1/4,1/4,1/4), respectively, and leaving the position (3/4,3/4,3/4) vacant. Among hH-alloys, the (Ti,Zr,Hf)NiSn systems have been extensively studied and are considered promising candidates within the n-type semiconductors for thermoelectric applications. Machine learning studies still emphasize the potential of half-Heusler alloys, particularly (Ti,Zr,Hf) NiSn [6].

Despite the promising nature of hH alloys as TE materials, there are significant challenges that need to be addressed for their industrial scale-up implementation. One of the main hurdles is their relatively high thermal conductivity when compared to other TE materials such as skutterudittes [7]. To mitigate this limitation, various approaches have been explored, such as introducing mass contrast [8–10] or nanostructuring techniques [11–13]. These methods offer the potential to transform hH alloys into viable alternatives to the exiting TE materials. In particular, severe plastic deformation achieved through high-pressure torsion has proven to be effective in significantly reducing the thermal conductivity in p- and n-type TE materials [14–16]. In contrast, recent studies indicate that chemical doping has limited impact on reducing the thermal conductivity [17]. Additionally, a crucial parameter for the design of industrial-scale TE generators is the linear coefficient of thermal expansion (CTE). Since these materials are intended for use across a wide temperature range, it is essential to control the mismatch between components, such as semiconductors and substrates [18]. In TE applications, the maximum operating temperature typically falls within the range of 500–1000 K [2]. The linear CTE, α, is defined as:

$$\alpha = \frac{1}{a}\left(\frac{\Delta a}{\Delta T}\right), \quad (2)$$

where a represents the lattice parameter at a certain temperature and Δa corresponds to the change in lattice parameter due to a temperature variation, ΔT. While there are limited reports on the temperature-dependent thermomechanical properties of TE materials [19] and on the CTE [20,21], most of these studies have relied on dilatometry [20,22]. High temperature X-ray powder diffraction (XRPD) data, which provide a direct method for determining lattice parameter at elevated temperatures are scarce [21,23]. However, such data are crucial for understanding thermal expansion and other thermomechanical properties, particularly in the context of building a TE modules or generators [1,24], as well as considering the oxidation of these modules at high temperatures [25]. Therefore, a comprehensive and precise understanding of the physical behavior of potential TE material candidates with respect to temperature is essential.

In this paper we investigate the thermal expansion coefficient of a (M,M',M")NiSn (M, M',M" = Ti, Zr, Hf) series of half-Heusler alloys by means of temperature dependent high resolution synchrotron radiation X-ray powder diffraction and the relationship of this parameter to others such as the Debye temperature, in addition to the implications it may have in transport properties.

2. Methods

Polycrystalline samples of hH compounds, with nominal compositions TiNiSn, ZrNiSn, HfNiSn, $Hf_{0.5}Zr_{0.5}NiSn$, $Hf_{0.5}Ti_{0.5}NiSn$, $Ti_{0.5}Zr_{0.5}NiSn$ and $Ti_{0.5}Hf_{0.25}Zr_{0.25}NiSn$, were prepared by arc melting. Elemental precursors (Ni, Sn, Zr – Goodfellow; Hf, Ti – Alpha Aesar, purity > 99.5%) were arc melted in the desired stoichiometric ratios. To enhance sample homogeneity, the ingots were flipped over multiple times and remelted. Subsequently, the ingots were crushed to powder, sealed in an evacuated quartz ampoules under Ar atmosphere, annealed at 1123 K for one week and eventually ice-water quenched.

High resolution synchrotron radiation X-ray powder diffraction (SR-XRPD) patterns of the heat-treated samples were collected at the ID22 beamline (ESRF, Grenoble, France), at various temperatures (300, 450, 600, 675, 750, 825 and 900 K), in the 2θ = 1–66º angular range, using a 62 keV energy beam. Wavelength calibration (λ = 0.2000 Å) at room temperature was performed using a Silicon standard sample. The powder samples were placed in sealed 0.3 mm diameter boron-glass capillaries, which were mounted in a goniometer and rotated to improve powder averaging, thereby minimizing texture and preferential orientations. All the collected patterns were analyzed using the Rietveld method implemented in the Fullprof Suite[26]. A Thomson-Cox-Hastings pseudo-Voigt peak shape function was employed to model the Bragg diffraction profiles. The quality of the refinement was assessed using the Bragg factor R_B, which measures the agreement between the refinement and the experimental data for each phase.

3. Results and discussion

The high-resolution SR-XRPD patterns of the ternary alloys, collected at room temperature (RT), along with the corresponding Rietveld fits are shown in Fig. 1. The observed peaks in all three samples can be indexed as Bragg reflections belonging to a majority phase (> 90 wt%) with a cubic crystal structure (space group F-43m). This major phase corresponds to the expected hH MNiSn phase, with slight variations in lattice parameter values depending on the M element. Specifically, the lattice parameters are found to be a = 5.9291(2) Å for TiNiSn, a = 6.1072(1) Å for ZrNiSn and a = 6.0764(1) Å for HfNiSn. These values are in good agreement with previously reported data (a = 5.9372 Å, a = 6.11173(2) Å and a = 6.07668(9) Å, for M = Ti, Zr and Hf, respectively) [27–29]. The insets in Fig. 1 clearly show that the most intense peak corresponds to a single Bragg reflection, indicating the presence of single crystalline hH phases in these MNiSn alloys.

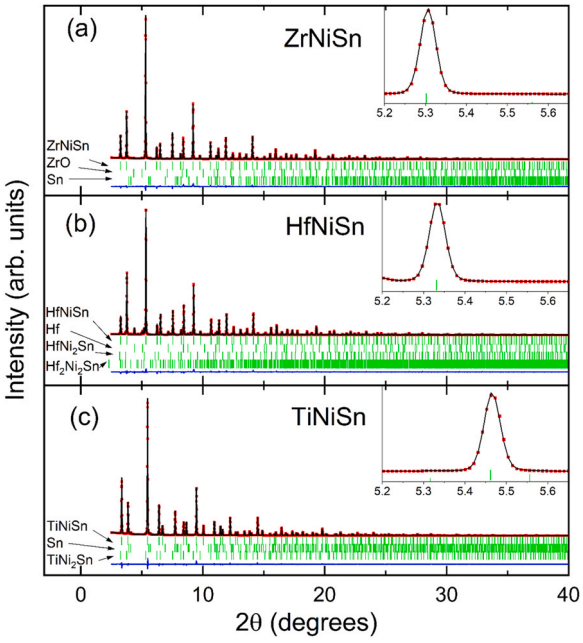

Fig. 1. Observed (red dots) and calculated (solid black line) room temperature HR SR-XRPD patterns of the ternary MniSn (M = (a) Ti, (b) Zr or (c) Hf) half-Heusler alloys. The solid blue line below each pattern is the difference between the experimental and the calculated data. Bragg reflections of the hH alloys and the secondary phases are represented as green vertical lines. The peak corresponding to the (220) Bragg reflection is depicted in the inset for each alloy, indicating a single hH phase.

Table 1
Structural parameters (for those phases with abundance > 3 wt%), obtained by Rietveld refinement of the HR SR-XRPD patterns, at RT, for the ternary MNiSn hH alloys. Detailed information on all phases in each sample is presented in Table S1 of the Supplementary Material.

Sample	Phases	Space group	Abundance (%)	Lattice parameter (Å)	R_B (%)
TiNiSn	TiNiSn	*F*-43*m*	98.2(1.3)	5.9291(2)	4.45
	Minority phases		1.8(3)		
ZrNiSn	ZrNiSn	*F*-43*m*	98.5(1.0)	6.1072(1)	4.45
	Minority phases		1.5(2)		
HfNiSn	HfNiSn	*F*-43*m*	92.0(5)	6.0764(1)	3.99
	Hf	*Fm*-3*m*	3.39(8)	4.5223(2)	19.6
	$HfNi_2Sn$	*Fm*-3*m*	4.44(13)	6.2371(3)	16.3
	Minority phases		0.21(9)		

Table 1 presents the structural parameters and phase percentages for the hH alloys, including the identification of small amounts of other minority phases. The lattice parameters follow the trend $a_{ZrNiSn} > a_{HfNiSn} > a_{TiNiSn}$, which is consistent with the larger the atomic radii leading to larger parameters, as reported in the literature [27]. The importance of using an experimental technique such as high-resolution XRPD to achieve precise analysis of the crystal structure is worth highlighting. In a previous study, the same samples were measured at room temperature and reported in Ref. [27] using higher resolution. It is noteworthy that the ZrNiSn alloy exhibited a split in every Bragg peak associated with the hH crystal structure, indicating phase segregation. However, this feature was not observed in the current study.

In the case of quaternary and quinary alloys, where the M site contains two or three atomic species, we observed different scenarios regarding the existence of hH phases:

(i) Zr-Hf-Ni-Sn: A single hH phase was observed, consistent with previous findings in the literature [30].
(ii) Ti-Hf-Ni-Sn and Ti-Zr-Hf-Ni-Sn: Two phases were identified, indicating phase segregation. This observation is also in agreement with previous reports, which have shown that the addition of Ti promotes phase separation [31].
(iii) Ti-Zr-Ni-Sn: Four phases were detected, further confirming phase segregation in this alloy system.

Minority phases, such as Hf_5Sn_4 and Sn_5Ti_6 were also observed but their contribution to the overall composition was low (≤3%). Interestingly, the experimental procedure used in this study yielded a higher percentage of hH phases compared to other reports. The detailed composition and abundance of each hH and minority phases, obtained through Rietveld refinements, can be found in Tables S1 and S2 of the Supplementary Material.

The composition values of the hH phases generally agree well with those calculated using Vegard's rule [32] (using the lattice parameters in Table 1), as specified in detail in the Supplementary Material. It should be noted that the lattice parameters and phase compositions can be determined with high precision through Rietveld refinements. For the purpose of this study, we consider the phase compositions obtained by Vegard's law, as depicted in Table 2, to be the correct values hereinafter.

The linear CTE, α, was determined for the majority phases present in the hH alloys by utilizing Eq. (1). The temperature-dependent lattice parameter is shown in Fig. 2 for each phase. The compositions for quaternary and quinary alloys were obtained through Rietveld refinements (see Table 2). Within the temperature range of the experiments (300–900 K), a linear trend was observed for all the phases, allowing for the assumption of constant CTE values (see Table 3). For instance, in this study, a value of $\alpha_{ZrNiSn} = 0.86(1) \times 10^{-5}$ K^{-1} was obtained, which is reasonably consistent with the theoretical CTE value of $\alpha = 0.78 \times 10^{-5}$ K^{-1} [33] for ZrNiSn, determined using a quasiharmonic approximation within the density functional theory (DFT) and employing a supercell-FDM approach. Comparatively, other families of thermoelectric compounds, such as skutterudites, clathrates and BiTe have higher CTEs, while oxides generally present lower values (with some exceptions) [34].

The thermal expansion of the investigated ternary alloys decreases with the atomic mass of the M atom; hence $\alpha_{TiNiSn} > \alpha_{ZrNiSn} > \alpha_{HfNiSn}$. From a microscopic point of view, the temperature dependence of bond relaxation, as well as that of the lattice parameter, is usually attributed to the anharmonicity of the interatomic potential [35]. In this respect, the CTE is analogous to the temperature-dependent specific heat: $\alpha(T) = B(r)C_V(T)$. At high temperatures, B (r) can be approximated as constant, leading to a direct proportionality between CTE and specific heat. Notably, both CTE and specific heat tend to remain constant at elevated temperatures. On the other hand, the Debye temperature is related to several physical properties, such as the specific heat and melting temperature. Consequently, it is possible to establish a close relationship between the CTE and the Debye temperature.

The Debye temperature is indeed connected to the vibrational properties of a crystal [36]. In Rietveld refinements, we can account for thermal vibrations by fitting the parameter B_{iso}, which corresponds to the atomic displacement parameters (ADPs). In the cubic cell, we considered isotropic ADPs ($< U_{iso}^2 >$), for each atom, assuming the same displacements in all directions. ADPs may also provide information about the disorder within the crystal structure. Rietveld refinement provides the temperature factors B_{iso} for each atom, being

$$B_{iso} = 8\pi^2 < U_{iso}^2 > \quad (3)$$

which considers both the atomic displacement parameters ($< U_{iso}^2 >$) and a component related to the static disorder (B_{sta}) present in the alloys [37]. The value of the $< U_{iso}^2 >$ corresponding to a specific compound is determined as the weighted average of $< U_{iso}^2 >$ for each atomic species within each phase. This calculation takes into account the obtained composition using Vegard's law, as explained above. Fig. 3 illustrates the experimental isotropic ADPs ($< U_{iso}^2 >$) for the ternary alloys MNiSn (M = Ti, Zr, Hf) as a function of temperature for each composition.

The atomic displacement parameters were analyzed using the Debye model for simple crystal structures [38,39], assuming a single mass, *m*, that corresponds to the weighted average mass of every atomic species, taking into account the occupancy fractions. Quantitative information about the temperature-dependent isotropic parameters can be obtained by fitting the experimental $< U_{iso}^2 >$ to the Debye model [40]:

$$< U_{iso}^2 > = \frac{3\hbar^2 T}{m k_B \theta_D^2} \left[\frac{T}{\theta_D} \int_0^{\frac{\theta_D}{T}} \frac{x}{e^x - 1} dx + \frac{\theta_D}{4T} \right] \quad (4)$$

where $\hbar$ represents the reduced Planck constant, k_B *is* the Boltzmann constant, *m* is the averaged mass, θ_D is the Debye temperature and T is the absolute temperature. The experimental $< U_{iso}^2 >$ was fitted to Eq. (4) allowing us to estimate the Debye temperature. The refined values of the Debye temperature are presented in Table 3. The Debye temperature generally depends on temperature and can be calculated using the Thirring-Stern expansions of the quasiharmonic expression for a thermodynamic function, such as the thermal energy W_{th}^h [41]. In this case, the quasiharmonic Debye temperature for the thermal energy θ_W^h can be expressed as:

$$\theta_W^h = \theta_1 + \sum_{n=1}^{\infty} b_n T^{-n}, \quad (5)$$

Table 2
Structural parameters, obtained by the Rietveld refinement of the HR SR-XRPD patterns, at RT, for the quaternary and quinary (M,M',M'')NiSn hH alloys. Note that the phases compositions here were obtained by Vegard's law. Information on all phases in each sample is presented in Table S2 of the Supplementary Material.

Sample	Phase composition	Space group	Abundance (%)	Lattice parameter (Å)	R_B (%)
$Zr_{0.5}Hf_{0.5}NiSn$	$Zr_{0.53(3)}Hf_{0.47(2)}NiSn$	*F*-43*m*	95(2)	6.0908(1)	5.76
	Hf_5Sn_4	*P*6$_3$/*mcm*	3.2(2)	8.699(4); 5.911(4)	11.5
	Minority phases		1.4(2)		
$Ti_{0.5}Hf_{0.5}NiSn$	$Ti_{0.700(13)}Hf_{0.300(13)}NiSn$	*F*-43*m*	36.0(1.3)	5.9732(3)	1.88
	$Ti_{0.300(6)}Hf_{0.700(6)}NiSn$	*F*-43*m*	63(3)	6.0321(1)	1.82
	Minority phases		0.68(0.4)		
$Ti_{0.5}Zr_{0.5}NiSn$	$Ti_{0.814(15)}Zr_{0.186(15)}NiSn$	*F*-43*m*	8.3(6)	5.962(1)	3.77
	$Ti_{0.668(5)}Zr_{0.332(5)}NiSn$	*F*-43*m*	21.4(9)	5.991(3)	2.90
	$Ti_{0.306(6)}Zr_{0.694(6)}NiSn$	*F*-43*m*	50.0(8)	6.0548(16)	4.02
	$Ti_{0.099(5)}Zr_{0.901(5)}NiSn$	*F*-43*m*	20.3(4)	6.0902(4)	4.33
	Minority phases		2.1(9)		
$Ti_{0.5}Zr_{0.25}Hf_{0.25}NiSn$	$Ti_{0.310(10)}Zr_{0.345(5)}Hf_{0.345(5)}NiSn$	*F*-43*m*	68.7(1.0)	6.0409(1)	1.93
	$Ti_{0.732(18)}Zr_{0.134(9)}Hf_{0.134(9)}NiSn$	*F*-43*m*	29.3(8)	5.9725(2)	2.96
	Minority phases		2.0(2)		

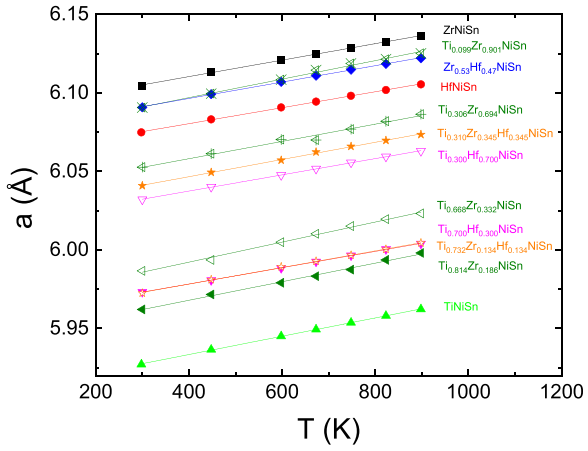

Fig. 2. Temperature dependence of the lattice parameter for each phase within the investigated hH alloys. Lines correspond to linear fittings, from which the linear CTE was estimated from Eq. (1). It is worth noting that error bars are on the order of graph point size.

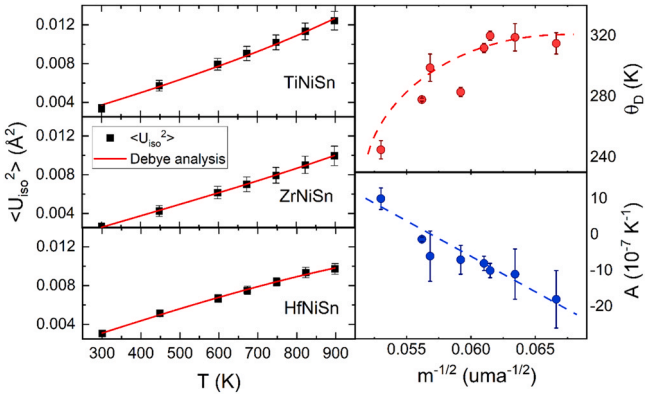

Fig. 3. (Left) Temperature dependent isotropic ADPs $< U_{iso}^2 >$ for the experimental and calculated $< U_{iso}^2 >$ (see text), for the ternary alloys. (Right) Molar mass dependent Debye temperature, θ_D, and anharmonicity, *A*, values for the ternary alloys, obtained from the fittings of the experimental $< U_{iso}^2 >$ values to the Debye analyses, i.e. Eq. (3). For the quaternary alloys, the analyses were identical, and the Debye analyses (following Eq. (3)) yielded the values of θ_D *and A* presented in Table 3. The dashed lines are guides for the eyes. Error bars on $< U_{iso}^2 >$ correspond to propagating errors from B_{iso} parameters obtained by Rietveld refinements. θ_D and *A* errors were calculated from propagating errors from the fitting of $< U_{iso}^2 >$ values to Eq. (4).

where b_n are coefficients (see Ref. [41]) and θ_n correspond to the characteristic temperatures, associated with the vibrational frequencies of the solid. When the characteristic temperatures reach the value of the Debye temperature, the Debye expansion is obtained. However, not only the quasiharmonic term, but also an anharmonic contribution should be included. Therefore, the temperature-dependent Debye temperature can be calculated as:

$$\theta_W = \theta_W^h + \left[\frac{1}{2} A T^2 \Big/ \frac{d\left(\frac{W_{th}^h}{3Nk_BT}\right)}{d\left(\frac{\theta_W^h}{T}\right)} \right] \quad (6)$$

where the coefficient A can be understood as an anharmonicity contribution, subject to the condition $|AT| < 1$ to ensure its validity. ADP values were fitted to Eq. (4), using the T-dependent θ_D obtained from Eq. (6), as shown in Fig. 3 for the ternary alloys (and in Fig. S3 in the Supplementary Material for the quaternary and quinary compositions). The extracted values of the Debye temperature (θ_1, hereinafter referred to as θ_D) and the anharmonicity parameter, *A*, from these fittings, are provided in Table 3. The dependence of θ_D and *A* on the molar mass of the alloys is depicted in the insets of Fig. 3. A clear trend is observed, with the anharmonicity parameter,

Table 3
Linear CTE for the (M,M',M'')NiSn hH alloys, for each phase. In this case, we show the refined composition, obtained by Rietveld refinement of the XRD data (see Tables 1 and 3), as the linear CTE behaves differently for each phase. Debye temperatures, θ_D, and the anharmonicity factor, A, are obtained from fittings of temperature-dependent ADPs to Eq. (3), together with the R^2 goodness-of-fits. The values of θ_D are compared to other values reported in the literature.

Phase composition	α (10^{-5} K^{-1})	θ_D (K) This study	θ_D (K) Previous studies	A (10^{-7} K^{-1})	R^2
TiNiSn	0.983(8)	315(7)	384 [4] 404.86 [34]	-14(8)	0.99491
ZrNiSn	0.86(1)	312(3)	398 [4] 333.39 [34]	-8(2)	0.99966
HfNiSn	0.838(9)	254(6)	348 [4] 306.32 [34]	9(4)	0.99707
$Zr_{0.53(3)}Hf_{0.47(2)}NiSn$	0.86(1)	298(9)		-6(7)	0.99593
$Ti_{0.300(6)}Hf_{0.700(6)}NiSn$	0.859(5)	272(4)	334.36 [35]	-0.03(8)	0.99938
$Ti_{0.700(13)}Hf_{0.300(13)}NiSn$	0.871(5)	315(4)		-8(3)	0.99993
$Ti_{0.310(1)}Zr_{0.345(1)}Hf_{0.345(1)}NiSn$	0.909(15)	278(4)		1.5(2.6)	0.99734
$Ti_{0.732(1)}Zr_{0.134(1)}Hf_{0.134(1)}NiSn$	0.888(12)	311(9)		-8(7)	0.99740

A, decreasing with $1/\sqrt{m}$, indicating that lighter compounds exhibit lower anharmonicity. Additionally, all the values for A are very small compared to those found in the literature [40], suggesting the presence of subtle anharmonic contributions to atomic vibrations.

Indeed, the phenomenon of thermal expansion cannot be fully explained by the solely considering the harmonic theory of a crystal lattice. An additional anharmonic term must be incorporated to account for the thermal expansion in crystals. Experimental techniques can provide valuable information about anharmonicity, including the temperature dependence of heat capacity and corresponding entropy curves. However, when dealing with powdery samples, obtaining precise measurements of these thermodynamic variables can be challenging. Nevertheless, alternative methods such as Raman spectroscopy offer insights into the anharmonic phonon behavior. By detecting shifts in the Raman frequency of phonons, it is possible to gather information about the effects of anharmonicity. Additionally, density functional theory (DFT) calculations can be employed to calculate the phonon dispersion curves and phonon lifetimes, which further contribute to understanding the anharmonic behavior in the crystal.

Table 3 and Fig. 4 demonstrate a correlation between θ_D and the thermal expansion α. In most cases, a higher α corresponds to a greater θ_D (the latter corresponding to the lighter compounds, i.e., TiNiSn). It is well-established that lower θ_D values are associated with lower the thermal conductivity (κ) [42]. θ_D can be regarded as a limit of lattice stability, enabling electrons to move through the lattice planes with minimal scattering due to the low electron-phonon coupling. Above θ_D, scattering increases, resulting in a reduction in κ. Recent studies have explored the role of the anharmonicity in thermoelectric properties [42]. By combining theory and experiment, researchers have revealed how a strong phonon anharmonicity can lead to intrinsically low lattice conductivity. This finding supports the notion that anharmonicity influences the vibrational modes, suppressing phonon thermal transport and providing insights for the design of efficient thermoelectric materials with low κ [35]. Examples of this are the recent studies on various thermoelectric materials, including InTe [34], BiTe-based compounds [43], Cu-chalcogenides [44], $Mg_3(Sb,Bi)_2$ [45] and oxychalcogenides [46]. Indeed, it is reasonable to anticipate that phases with lower thermal expansion coefficients, indicating higher anharmonicity, would exhibit lower lattice thermal conductivity, which is an advantage in terms of the efficiency of TE materials, as the figure of merit is inversely proportional to κ.

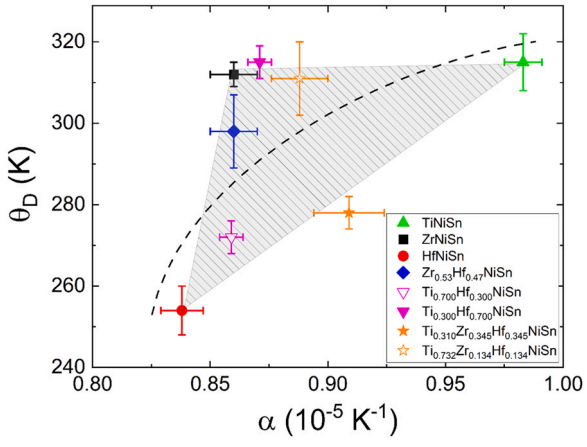

Fig. 4. Debye temperature vs. linear coefficient of thermal expansion for (M,M',M'') NiSn (M,M',M''=Ti,Zr,Hf). Note that the composition of the alloy follows the same color-symbol code as in Fig. 2. The dashed line is a guide for the eyes. Error bars on the thermal expansion were calculated from propagating errors from experimental uncertainties of related magnitudes and those in the Debye temperatures from propagating errors from the fitting of $< U_{iso}^2 >$ values to Eq. (4).

In this regard, we attempt to establish an initial correlation between thermal conductivity and Debye temperature in the investigated compositions. This correlation is also compared to other families of thermoelectric materials, as shown in Fig. S4 of the Supporting information. The reported values of lattice thermal conductivity at room temperature further support this idea: 9.3 $W{\cdot}K^{-1}{\cdot}m^{-1}$ for TiNiSn, 8.8 $W{\cdot}K^{-1}{\cdot}m^{-1}$ for ZrNiSn and 6.7 $W{\cdot}K^{-1}{\cdot}m^{-1}$ for HfNiSn [47]; hence $\kappa_{HfNiSn} < \kappa_{ZrNiSn} < \kappa_{TiNiSn}$, which aligns with the trend observed in the CTE and the θ_D. In this respect, it is worth noting that, in the search for TE materials with promising properties, such as a large thermoelectric figure of merit zT, the focus should be on materials with low thermal conductivity, which would exhibit large anharmonicity effects, as observed in the current study.

4. Conclusions

From high resolution SR-XRPD experiments on hH (M, M', M'') NiSn alloys, with M, M', M'' = Ti, Zr, Hf, several conclusions can be drawn. Firstly, single phases were identified for the ternary and quaternary based on Zr and/or Hf alloys, namely ZrNiSn, HfNiSn, and (Zr,Hf)NiSn. These alloys exhibit significant anharmonic effects, as evidenced by their low linear coefficients of thermal expansion ($\alpha < 10^{-5}$ K^{-1}) and Debye temperatures (250–320 K). Secondly, for the (Ti,Hf)NiSn and (Ti,Zr,Hf)NiSn alloys, two hH phases were observed, with slightly higher linear coefficients of thermal compared to the single phases but still below 10^{-5} K^{-1}. Additionally, the (Ti,Zr)NiSn alloy exhibited at least four hH phases. The close correlation between the linear coefficient of thermal expansion and the Debye temperature in the (Ti,Zr,Hf)NiSn alloys suggests that other properties, such as thermal conductivity, may also be similarly correlated. These findings support the notion that anharmonicity plays a crucial role in thermal properties of these alloys and could serve as a key parameter in the search for prospective thermoelectric materials. However, further in-depth exploration is necessary to fully comprehend the physical properties of these alloys.

CRediT authorship contribution statement

C. Echevarria-Bonet: Investigation, Data curation, Writing – original draft. **J. L. Garrido**: Data curation. **D. Martinez-Blanco**: Data curation, Formal analysis. **P. Gorria**: Writing – review & editing. **M. H. Sørby**: Data curation. **M. D. Riktor**: Investigation. **J. A. Blanco**: Writing – review & editing. **B. C. Hauback**: Supervision.

Data Availability

Data will be made available on request.

Declaration of Competing Interest

The authors declare that they have no known competing financial interests or personal relationships that could have appeared to influence the work reported in this paper.

Acknowledgments

This work was funded by the Research Council of Norway within the THELMA project (No. 228854) and Principado de Asturias (IDI/2018/000185 and SV-PA-21-AYUD/2021/51822) projects. The authors acknowledge the skillful assistance of the staff at ID22 beamline, at ESRF, Grenoble, France and the technical support provided by Servicios Científico-Técnicos de la Universidad de Oviedo. The work of C. Echevarria-Bonet was partially supported by Banco Santander via a mobility grant for professors and researchers from the University of Oviedo (2021–2022).

Appendix A. Supporting information

Supplementary data associated with this article can be found in the online version at doi:10.1016/j.jallcom.2023.170583.

References

[1] M. Jiang, Y. Fu, Q. Zhang, Z. Hu, A. Huang, S. Wang, L. Wang, W. Jiang, High-efficiency and reliable same-parent thermoelectric modules using Mg_3Sb_2-based compounds, Natl. Sci. Rev. 10 (2023) nwad095, https://doi.org/10.1093/NSR/NWAD095

[2] Z. Wu, S. Zhang, Z. Liu, E. Mu, Z. Hu, Thermoelectric converter: strategies from materials to device application, Nano Energy 91 (2022) 106692, , https://doi.org/10.1016/J.NANOEN.2021.106692

[3] Publications Office of the EU, Assessment of the Methodology for Establishing the EU List of Critical Raw Materials - Annexes. EUR 28654 EN, 2017. https://doi.org/10.2760/875135.

[4] European Commission, Critical Raw Materials Resilience: Charting a Path towards greater Security and Sustainability, 2020. https://eur-lex.europa.eu/legal-content/EN/TXT/HTML/?uri=CELEX:52020DC0474&from=EN.

[5] X. Zhang, S. Li, B. Zou, P. Xu, Y. Song, B. Xu, Y. Wang, G. Tang, S. Yang, Significant enhancement in thermoelectric properties of half-Heusler compound TiNiSn by grain boundary engineering, J. Alloy. Compd. 901 (2022) 163686, , https://doi.org/10.1016/J.JALLCOM.2022.163686

[6] X. Jia, Y. Deng, X. Bao, H. Yao, S. Li, Z. Li, C. Chen, X. Wang, J. Mao, F. Cao, J. Sui, J. Wu, C. Wang, Q. Zhang, X. Liu, Unsupervised machine learning for discovery of promising half-Heusler thermoelectric materials, NPJ Comput. Mater. 8 (2022) 34, https://doi.org/10.1038/s41524-022-00723-9

[7] A. Serrano, O. Caballero-Calero, C. Granados-Miralles, G. Gorni, C.V. Manzano, M. Rull-Bravo, A. Moure, M. Martín-González, J.F. Fernández, $CoSb_3$-based skutterudite nanocomposites prepared by cold sintering process with enhanced thermoelectric properties, J. Alloy. Compd. 931 (2023) 167534, , https://doi.org/10.1016/J.JALLCOM.2022.167534

[8] N.S. Chauhan, Y. Miyazaki, Contrasting role of bismuth doping on the thermoelectric performance of VFeSb half-Heusler, J. Alloy. Compd. 908 (2022) 164623, , https://doi.org/10.1016/J.JALLCOM.2022.164623

[9] R. Gurunathan, S. Sarker, C.K.H. Borg, J. Saal, L. Ward, A. Mehta, G.J. Snyder, R. Gurunathan, G.J. Snyder, S. Sarker, A. Mehta, C.K.H. Borg, J. Saal, L. Ward, Mapping thermoelectric transport in a multicomponent alloy space, Adv. Electron. Mater. 8 (2022) 2200327, https://doi.org/10.1002/AELM.202200327

[10] B. Jiang, W. Wang, S. Liu, Y. Wang, C. Wang, Y. Chen, L. Xie, M. Huang, J. He, High figure-of-merit and power generation in high-entropy GeTe-based thermoelectrics, Science 377 (2022) 208–213, https://doi.org/10.1126/SCIENCE.ABQ5815

[11] A. Kumar, S. Bano, B. Govind, A. Bhardwaj, V.N. Singh, Enhanced thermoelectric performance of n-type $Zr_{0.66}Hf_{0.34}Ni_{1+x}Sn$ Heusler nanocomposites, J. Alloy. Compd. 900 (2022) 163454, , https://doi.org/10.1016/J.JALLCOM.2021.163454

[12] A. Karati, S. Ghosh, M. Nagini, R.C. Mallik, R. Shabadi, B.S. Murty, U.V. Varadaraju, Thermoelectric properties of nanocrystalline half-Heusler high-entropy $Ti_2NiCoSn_{1-x}Sb_{1+x}$ (x = 0.3, 0.5, 0.7, 1) alloys with VEC > 18, J. Alloy. Compd. 927 (2022) 166578, , https://doi.org/10.1016/J.JALLCOM.2022.166578

[13] C. Hu, K. Xia, C. Fu, X. Zhao, T. Zhu, Carrier grain boundary scattering in thermoelectric materials, Energy Environ. Sci. 15 (2022) 1406–1422, https://doi.org/10.1039/D1EE03802H

[14] G. Rogl, S. Ghosh, L. Wang, J. Bursik, A. Grytsiv, M. Kerber, E. Bauer, R.C. Mallik, X.Q. Chen, M. Zehetbauer, P. Rogl, Half-Heusler alloys: Enhancement of ZT after severe plastic deformation (ultra-low thermal conductivity), Acta Mater. 183 (2020) 285–300, https://doi.org/10.1016/J.ACTAMAT.2019.11.010

[15] K. Edalati, A. Bachmaier, V.A. Beloshenko, Y. Beygelzimer, V.D. Blank, W.J. Botta, K. Bryła, J. Čížek, S. Divinski, N.A. Enikeev, Y. Estrin, G. Faraji, R.B. Figueiredo, M. Fuji, T. Furuta, T. Grosdidier, J. Gubicza, A. Hohenwarter, Z. Horita, J. Huot, Y. Ikoma, M. Janeček, M. Kawasaki, P. Král, S. Kuramoto, T.G. Langdon, D.R. Leiva, V.I. Levitas, A. Mazilkin, M. Mito, H. Miyamoto, T. Nishizaki, R. Pippan, V.V. Popov, E.N. Popova, G. Purcek, O. Renk, Á. Révész, X. Sauvage, V. Sklenicka, W. Skrotzki, B.B. Straumal, S. Suwas, L.S. Toth, N. Tsuji, R.Z. Valiev, G. Wilde, M.J. Zehetbauer, X. Zhu, Nanomaterials by severe plastic deformation: review of historical developments and recent advances, Mater. Res. Lett. 10 (2022) 163–256, https://doi.org/10.1080/21663831.2022.2029779

[16] K. Fukuta, K. Tsuchiya, H. Miyazaki, Y. Nishino, Improving thermoelectric performance of Fe_2VAl-based Heusler compounds via high-pressure torsion, Appl. Phys. A Mater. Sci. Process 128 (2022) 1–8, https://doi.org/10.1007/S00339-022-05329-Y

[17] Q. Ren, C. Fu, Q. Qiu, S. Dai, Z. Liu, T. Masuda, S. Asai, M. Hagihala, S. Lee, S. Torri, T. Kamiyama, L. He, X. Tong, C. Felser, D.J. Singh, T. Zhu, J. Yang, J. Ma, Establishing the carrier scattering phase diagram for ZrNiSn-based half-Heusler thermoelectric materials, Nat. Commun. 11 (2020) 3142, https://doi.org/10.1038/s41467-020-16913-2

[18] R. Liu, Y. Xing, J. Liao, X. Xia, C. Wang, C. Zhu, F. Xu, Z.G. Chen, L. Chen, J. Huang, S. Bai, Thermal-inert and ohmic-contact interface for high performance half-Heusler based thermoelectric generator, Nat. Commun. 13 (2022) 1–8, https://doi.org/10.1038/s41467-022-35290-6

[19] P. Sauerschnig, P. Jood, M. Ohta, P. Sauerschnig, P. Jood, M. Ohta, Improved high-temperature material stability and mechanical properties while maintaining a high figure of merit in nanostructured p-type pbte-based thermoelectric elements, Adv. Mater. Technol. 8 (2023) 2201295, https://doi.org/10.1002/admt.202201295

[20] G. Rogl, A. Grytsiv, M. Gürth, A. Tavassoli, C. Ebner, A. Wünschek, S. Puchegger, V. Soprunyuk, W. Schranz, E. Bauer, H. Müller, M. Zehetbauer, P. Rogl, Mechanical properties of half-Heusler alloys, Acta Mater. 107 (2016) 178–195, https://doi.org/10.1016/j.actamat.2016.01.031

[21] J.E.F.S. Rodrigues, J. Gainza, F. Serrano-Sánchez, R.S. Silva, C. Dejoie, N.M. Nemes, O.J. Dura, J.L. Martínez, J.A. Alonso, Thermal expansion and rattling behavior of Gd-Filled Co_4Sb_{12} skutterudite determined by high-resolution synchrotron x-ray diffraction, Materials 16 (2023) 370, https://doi.org/10.3390/ma16010370

[22] P. Hermet, R.M. Ayral, E. Theron, P.G. Yot, F. Salles, M. Tillard, P. Jund, Thermal expansion of Ni-Ti-Sn heusler and half-heusler materials from first-principles calculations and experiments, J. Phys. Chem. C. 118 (2014) 22405–22411, https://doi.org/10.1021/jp502112f

[23] D.A. Ferluccio, B.F. Kennedy, S.A. Barczak, S.R. Popuri, C. Murray, M. Pollet, J.-W.G. Bos, Thermal properties of TiNiSn and VFeSb halfHeusler thermoelectrics from synchrotron x-ray powder diffraction, J. Phys. Energy 3 (2021) 35001, https://doi.org/10.1088/2515-7655/abf41a

[24] F. Tohidi, S. Ghazanfari Holagh, A. Chitsaz, Thermoelectric generators: a comprehensive review of characteristics and applications, Appl. Therm. Eng. 201 (2022) 117793https://doi.org/10.1016/ j.applthermaleng.2021.117793.

[25] J. Gu, L. Wang, Q. Song, C. Wang, X. Xia, J. Liao, Y.Y. Sun, L. Chen, S. Bai, High-temperature oxidation mechanism of ZrCoSb-based half-Heusler thermoelectric compounds, J. Mater. Sci. Technol. 148 (2023) 242–249, https://doi.org/10.1016/J.JMST.2022.11.030

[26] J. Rodríguez-Carvajal, T. Roisnel, Line broadening analysis using fullprof: determination of microstructural properties, Mater. Sci. Forum 443 (2004) 123–126, https://doi.org/10.4028/www.scientific.net/msf.443-444.123

[27] M.N. Guzik, C. Echevarria-Bonet, M.D. Riktor, P.A. Carvalho, A.E. Gunnæs, M.H. Sørby, B.C. Hauback, Half-Heusler phase formation and Ni atom distribution in M-Ni-Sn (M = Hf, Ti, Zr) systems, Acta Mater. 148 (2018) 216–224, https://doi.org/10.1016/j.actamat.2018.01.019

[28] V.V. Romaka, P. Rogl, L. Romaka, Y. Stadnyk, A. Grytsiv, O. Lakh, V. Krayovskii, Peculiarities of structural disorder in Zr- and Hf-containing Heusler and half-Heusler stannides, Intermetallics 35 (2013) 45–52, https://doi.org/10.1016/j.intermet.2012.11.022

[29] T. Berry, C. Fu, G. Auffermann, G.H. Fecher, W. Schnelle, F. Serrano-Sanchez, Y. Yue, H. Liang, C. Felser, Enhancing thermoelectric performance of TiNiSn half-heusler compounds via modulation doping, Chem. Mater. 29 (2017) 7042–7048, https://doi.org/10.1021/acs.chemmater.7b02685

[30] J.W.G. Bos, R.A. Downie, Half-Heusler thermoelectrics: a complex class of materials, J. Phys.: Condens. Matter 26 (2014) 433201, , https://doi.org/10.1088/0953-8984/26/43/433201

[31] H. Geng, H. Zhang, Effects of phase separation on the thermoelectric properties of (Ti, Zr, Hf)NiSn half-Heusler alloys, J. Appl. Phys. 116 (2014) 033708, , https://doi.org/10.1063/1.4890610

[32] A.R. Denton, N.W. Ashcroft, Vegard's law, Phys. Rev. A 43 (1991) 3161, https://doi.org/10.1103/PhysRevA.43.3161

[33] S.S. Shastri, S.K. Pandey, Thermoelectric properties, efficiency and thermal expansion of ZrNiSn half-Heusler by first-principles calculations, J. Phys.: Condens. Matter 32 (2020) 355705, , https://doi.org/10.1088/1361-648X/AB8B9E

[34] D. Music, R.W. Geyer, P. Keuter, Thermomechanical response of thermoelectrics, Appl. Phys. Lett. 109 (2016) 223903, , https://doi.org/10.1063/1.4971387

[35] J. Zhang, D. Ishikawa, M.M. Koza, E. Nishibori, L. Song, A.Q.R. Baron, B.B. Iversen, Dynamic lone pair expression as chemical bonding origin of giant phonon anharmonicity in thermoelectric InTe, Angew. Chem., Int. Ed. 62 (2023) e202218458, , https://doi.org/10.1002/ANIE.202218458

[36] I. Skovsen, L. Bjerg, M. Christensen, E. Nishibori, B. Balke, C. Felser, B.B. Iversen, Multi-temperature synchrotron PXRD and physical properties study of half-Heusler TiCoSb, Dalton Trans. 39 (2010) 10154–10159, https://doi.org/10.1039/c0dt00742k

[37] Y. Xiao, Y. Su, R. Mittal, T. Chatterji, T. Hansen, S. Price, C.M.N. Kumar, J. Persson, S. Matsuishi, Y. Inoue, H. Hosono, T. Brueckel, Neutron diffraction study of phase transitions and thermal expansion of SrFeAsF, Phys. Rev. B 81 (2010) 094523, , https://doi.org/10.1103/PHYSREVB.81.094523

[38] A. Bentien, E. Nishibori, S. Paschen, B.B. Iversen, Crystal structures, atomic vibration, and disorder of the type-I thermoelectric clathrates $Ba_8Ga_{16}Si_{30}$, $Ba_8Ga_{16}Ge_{30}$, $Ba_8In_{16}Ge_{30}$, and $Sr_8Ga_{16}Ge_{30}$, Phys. Rev. B. 71 (2005) 144107, , https://doi.org/10.1103/PhysRevB.71.144107

[39] B.E. Warren, X-ray diffraction, Dover (1990).

[40] B.T.M. Willis, A.W. Pryor, Thermal vibrations in crystallography, Cambridge University Press, 1975.

[41] M.P. Tosi, F.G. Fumi, Temperature dependence of the debye temperatures for the thermodynamic functions of alkali halide crystals, Phys. Rev. 131 (1963) 1458.

[42] N.W. Ashcroft, N.D. Mermin, Solid State Physics, Saunders College Publishing, New York, 1976.

[43] R. Pathak, P. Dutta, A. Srivastava, D. Rawat, R.K. Gopal, A.K. Singh, A. Soni, K. Biswas, Strong Anharmonicity-Induced Low Thermal Conductivity and High n-type Mobility in the Topological Insulator $Bi_{1.1}Sb_{0.9}Te_2S$, Angew. Chem., Int. Ed. 61 (2022) e202210783, , https://doi.org/10.1002/ANIE.202210783

[44] T. Manimozhi, S. Kavirajan, S. Harish, J. Archana, K. Kamala Bharathi, E. Senthil Kumar, M. Navaneethan, Anharmonicity and low-thermal conductivity in the multi-phase composition of $Cu_3Bi_{0.75}Sb_{0.25}S_3$, Mater. Lett. 304 (2021) 130399, , https://doi.org/10.1016/J.MATLET.2021.130399

[45] J. Ding, T. Lanigan-Atkins, M. Calderón-Cueva, A. Banerjee, D.L. Abernathy, A. Said, A. Zevalkink, O. Delaire, Soft anharmonic phonons and ultralow thermal

conductivity in $Mg_3(Sb, Bi)_2$ thermoelectrics (eabg), Sci. Adv. 7 (2021) 1449, https://doi.org/10.1126/SCIADV.ABG1449

[46] J. Li, W. Zhai, C. Zhang, Y. Yan, P.F. Liu, G. Yang, Anharmonicity and ultralow thermal conductivity in layered oxychalcogenides BiAgOCh (Ch = S, Se, and Te), Mater. Adv. 2 (2021) 4876–4882, https://doi.org/10.1039/d1ma00375e

[47] H. Hohl, A.P. Ramirez, C. Goldmann, G. Ernst, B. Wölfing, E. Bucher, Efficient dopants for ZrNiSn-based thermoelectric materials, J. Phys. Condens. Matter 11 (1999) 1697, https://doi.org/10.1088/0953-8984/11/7/004